

DYNAMICAL FRICTION AND MEASUREMENTS OF THE SPLASHBACK RADIUS IN GALAXY CLUSTERS

TALIA M. O'SHEA^{1,2,3}, JOSH BORROW^{4,3}, STEPHANIE O'NEIL³, AND MARK VOGELSBERGER³

¹Department of Astronomy, University of Wisconsin–Madison, Madison, WI 53706, USA

²Department of Physics, Wellesley College, Wellesley, MA 02481, USA

³Department of Physics and Kavli Institute for Astrophysics and Space Research, Massachusetts Institute of Technology, Cambridge, MA 02139, USA

⁴Department of Physics and Astronomy, University of Pennsylvania, 209 South 33rd Street, Philadelphia, PA, USA 19104

Version May 30, 2024

ABSTRACT

The splashback radius is one popular method to constrain the size of galaxy clusters. It is typically measured through the logarithmic derivative of the galaxy number density profile, since doing so is more observationally viable and computationally inexpensive compared to other methods. However, measuring the splashback radius through the galaxy number density has consistently produced smaller values of the splashback radius than those measured with dark matter density or other processes. Dynamical friction has been posited as one possible reason that splashback radii measured through galaxy number densities are reduced, since it decays the orbits of subhaloes within the halo, however, the effects of dynamical friction cannot be isolated within cosmological simulations. Here, we present idealized simulations starting with isolated galaxy clusters drawn from the IllustrisTNG cosmological simulation, where we isolate dynamical friction. We show that although dynamical friction can reduce measurements of the splashback radius, it does not have a significant effect on clusters with $M_{200,\text{mean}} > 10^{14} M_{\odot}$, and thus cannot completely account for previously measured discrepancies.

Keywords: galaxies: clusters — methods: numerical

1. INTRODUCTION

The environment of the galaxy cluster is an incredibly challenging one to understand. Dominated by dark matter and the hot, gaseous, intracluster medium, it is notoriously difficult to observe. Galaxy clusters, the most massive gravitationally bound objects in the Universe, can have masses exceeding $10^{15} M_{\odot}$ and may contain anywhere from hundreds to hundreds of thousands of galaxies (henceforth called cluster galaxies; see e.g. Kravtsov & Borgani 2012, for a review). These resident cluster galaxies are typically much easier to observe than the underlying content of the cluster itself, thanks to their dominant stellar component. As such, they provide an excellent opportunity to understand the cluster environment through ensemble measurements of many galaxies.

Compared to the rest of the Universe, the cluster environment is dense and hot, which is the result of strong accretion shocks, and feedback from active galactic nuclei (AGN; see McNamara & Nulsen 2012; Kravtsov & Borgani 2012). On average, galaxies residing in clusters do not resemble their counterpart field galaxies (galaxies that do not reside in clusters or groups): they are typically redder and more elliptical (Dressler 1980; Hogg et al. 2004; Kauffmann et al. 2004; Blanton et al. 2005; Li et al. 2006), and have lower star formation rates (Poggianti et al. 1999; Gómez et al. 2003; O'Neil et al. 2023). Previous studies have sought to understand these differences, notably the rapid cessation of star formation (quenching) in galaxies as they fall into the cluster, identified for instance by the strength of the 4000Å break (Dressler & Shectman 1987; Kimble et al. 1989; Kauffmann et al. 2004; Li et al. 2006; Demarco et al. 2010; Bluck et al. 2020; Kim et al. 2022). One

explanation, known as “environmental quenching”, attributes the lack of star formation in cluster galaxies to a variety of processes that cause galaxies to lose their gas envelopes as they enter the cluster, such as ram pressure (seen observationally in Vollmer et al. 2004; Chung et al. 2009; Ebeling et al. 2014) and tidal stripping (Larson et al. 1980; Diemand et al. 2007).

Ram pressure stripping results from interactions between the hot cluster gas and the gas in an infalling galaxy, which removes gas from the galaxy and thus lowers star formation rates (Gunn & Gott 1972; Abadi et al. 1999; Poggianti et al. 1999), especially in the center of clusters (Wetzel et al. 2013; Borrow et al. 2023). Cluster galaxies are also impacted by tidal stripping, which is a gravitationally driven process in which mass at the edges of an infalling galaxy is pulled off. As a result, infalling galaxies lose mass, including gas. Tidal stripping has been observed in many N-body simulations (Dekel et al. 2003; Diemand et al. 2007), and like ram pressure stripping, is thought to operate most efficiently in the center of galaxy clusters (Moore et al. 1998). Subhaloes can also affect each other gravitationally in a process called harassment (Moore et al. 1998; Wetzel et al. 2013), or even merge.

Yet another process that occurs in the cluster environment is dynamical friction (DF; Chandrasekhar 1943; van den Bosch et al. 1999). Dynamical friction is a drag force that acts on objects (e.g. a subhalo) moving through a background comprised of particles (e.g. the cluster dark matter halo). Dynamical friction decays the orbit of the infalling object, with the effect strongest in this context on high-mass galaxies, causing them to merge with the central brightest central galaxy (BCG; Ostriker & Hausman 1977).

A foundational property of a galaxy cluster is its size. One common approach for measuring cluster size is to define a

*E-mail: tmoshea@wisc.edu

radius at which the average enclosed density is some multiple of the average density of the Universe. For instance, $R_{200,\text{mean}}$ refers to the radius at which the average enclosed density is two hundred times greater than the mean density of the Universe (Peebles 1993; Peacock 1999). The mass enclosed by $R_{200,\text{mean}}$ is accordingly referred to as $M_{200,\text{mean}}$. However, this metric is defined relative to the Universe as a whole. Thus, as the density of the Universe changes over cosmic time, $R_{200,\text{mean}}$ will change even if the cluster does not, a process known as pseudo-evolution (Diemer et al. 2013). Consequently, the value of $M_{200,\text{mean}}$ changes with time based on both the physical evolution of the cluster, and the evolution of the Universe at large.

To avoid pseudo-evolution, the splashback radius, or R_{sp} , has gained popularity in recent years. The splashback radius characterizes the size of the cluster based on the radius of the first apocenter of infalling material. This material produces a “pile-up” of matter around that first turn-around point due to the reduced velocity of subhaloes at their apocenters (Adhikari et al. 2021). As the splashback radius is defined with respect to the dynamics of the cluster, it does not experience pseudo-evolution.

The dynamical splashback feature is associated with a caustic in the density profile. In particular, the logarithmic density profile ($d\log\rho/d\log r$) exhibits a dip in the profile at this region. The local minimum of that feature marks an excellent proxy for R_{sp} (Diemer & Kravtsov 2014). Due to observational and computational challenges in finding the apocenters of numerous cluster galaxies or particles, the density profile is therefore a commonly used proxy for finding the splashback radius (see e.g. More et al. 2015; Chang et al. 2018; Shin et al. 2019; Murata et al. 2020; O’Neil et al. 2021, for examples).

For perfectly spherical systems, this caustic and the apocenter are well-matched (Adhikari et al. 2014; Mansfield et al. 2017). However, in reality, this correlation is not perfect. Clusters are not perfectly spherical – their density profiles are greatly influenced by their merger history (Diemer & Kravtsov 2014; Diemer 2017; Mansfield et al. 2017; Xhakaj et al. 2020), which can reduce the strength of the caustic. Nevertheless, because of its simplicity, the differential density profile remains the primary way of measuring R_{sp} .

Due to the long time scales involved in galaxy formation, numerical simulations have become an indispensable tool for understanding cluster evolution. Early dark matter-only simulations to investigate large-scale structure considered solely gravitational forces, and included only thousands of particles (Press & Schechter 1974; Davis et al. 1985). Dark matter simulations are thought to be extremely precise, because they include only gravitational forces (Springel 2010), however such simulations neglect many important processes, reducing their accuracy. The inclusion of baryonic matter introduces a tremendous challenge: simulating the numerous additional physical processes, such as hydrodynamics and radiative transfer, that this ordinary matter undergoes (Somerville & Davé 2015; Vogelsberger et al. 2020).

Modern cosmological N-body simulations can track dark matter, as well as gas, stellar, and supermassive black holes, through time. Newer simulations include increasingly complex interactions and processes that are thought to affect galaxy evolution and the formation of large-scale structure, such as feedback from AGN and massive stars (Crain et al. 2015; Schaye et al. 2015). There are many simulations that are large enough to include galaxy clusters, which have characteristic radii on the scale of 1 Mpc. By the 2010s, projects

such as Illustris and EAGLE reached simulation volumes of 106.5^3 and 100^3 Mpc³ respectively (Vogelsberger et al. 2014; Genel et al. 2014; Crain et al. 2015; Schaye et al. 2015), while resolving down to a “particle” mass scale of $\approx 10^6 M_{\odot}$ for baryonic components. Yet precisely replicating these feedback processes is persistently difficult, and mismatches with observational results remain.

Splashback radii have been measured in simulation data (Lau et al. 2015; More et al. 2016; Busch & White 2017; O’Neil et al. 2022), as well as in numerous observational projects using data from a variety of sources with different detection techniques, such as SDSS, DES, the Subaru Telescope, and ACT (More et al. 2016; Baxter et al. 2017; Chang et al. 2018; Shin et al. 2019; Zürcher & More 2019; Murata et al. 2020). Cluster splashback radii have been found to depend strongly on the accretion rate of the cluster, which refers to the rate at which the cluster gains mass (Diemer & Kravtsov 2014; Shin & Diemer 2023). Haloes with lower accretion rates possess larger splashback radii, relative to $R_{200,\text{mean}}$, than those with higher mass accretion rates (More et al. 2015).

Still, much about the exact position of R_{sp} remains unknown. Measuring the mass density profile of a halo, which is dominated by dark matter, is challenging in observation; ideally, the galaxy number density profile would act as a useful observational substitute for the dark matter density profile. However, simulations reveal a discrepancy between the dark matter density profile and the galaxy number density profile, affecting the position of the splashback radius. This disagreement has been identified in numerous simulations and observational studies (More et al. 2016; Bahé et al. 2019; O’Neil et al. 2021; McAlpine et al. 2022). Some researchers have posited that this discrepancy is due to dynamical friction. DF affects only the subhaloes (and the associated galaxies), reducing the extent of their orbits, but not the background dark matter. Therefore, it is a possible explanation for this discrepancy between the dark matter and galaxy density profiles.

For example, using a toy model, Adhikari et al. (2016) simulated dynamical friction in a galaxy cluster system, finding that DF reduced the splashback radius, when measured through galaxy number densities, in a spherical system where all galaxies moved in perfectly radial orbits. Adhikari et al. (2016) concluded not only that dynamical friction resulted in a noticeable decrease in R_{sp} for subhaloes above 1% of the host halo mass, but also that the influence of DF is highly dependent on the cluster potential profile.

Bahé et al. (2019) examined the Hydrangea simulations, part of the C-EAGLE project, and argue that the impact of dynamical friction is strongest among low-mass clusters. Xhakaj et al. (2020), also using simulations, found reduced splashback radii measured with subhalo profiles, which would be consistent with the impact of dynamical friction; however, they did not investigate the source of the discrepancy. McAlpine et al. (2022) presented results from SIBELIUS-DARK, that compared the differential density profiles of the dark matter particles to those of the member galaxies. They found that using the galaxies as tracers resulted in a splashback radius approximately 10% smaller than the radius measured with dark matter particles, and state that this is consistent with dynamical friction as the cause of this discrepancy.

However, some studies argue that dynamical friction’s influence is overstated. For example, Contigiani et al. (2019) state that dynamical friction is insignificant at splashback scales. van den Bosch et al. (2016) argue that DF is only significant

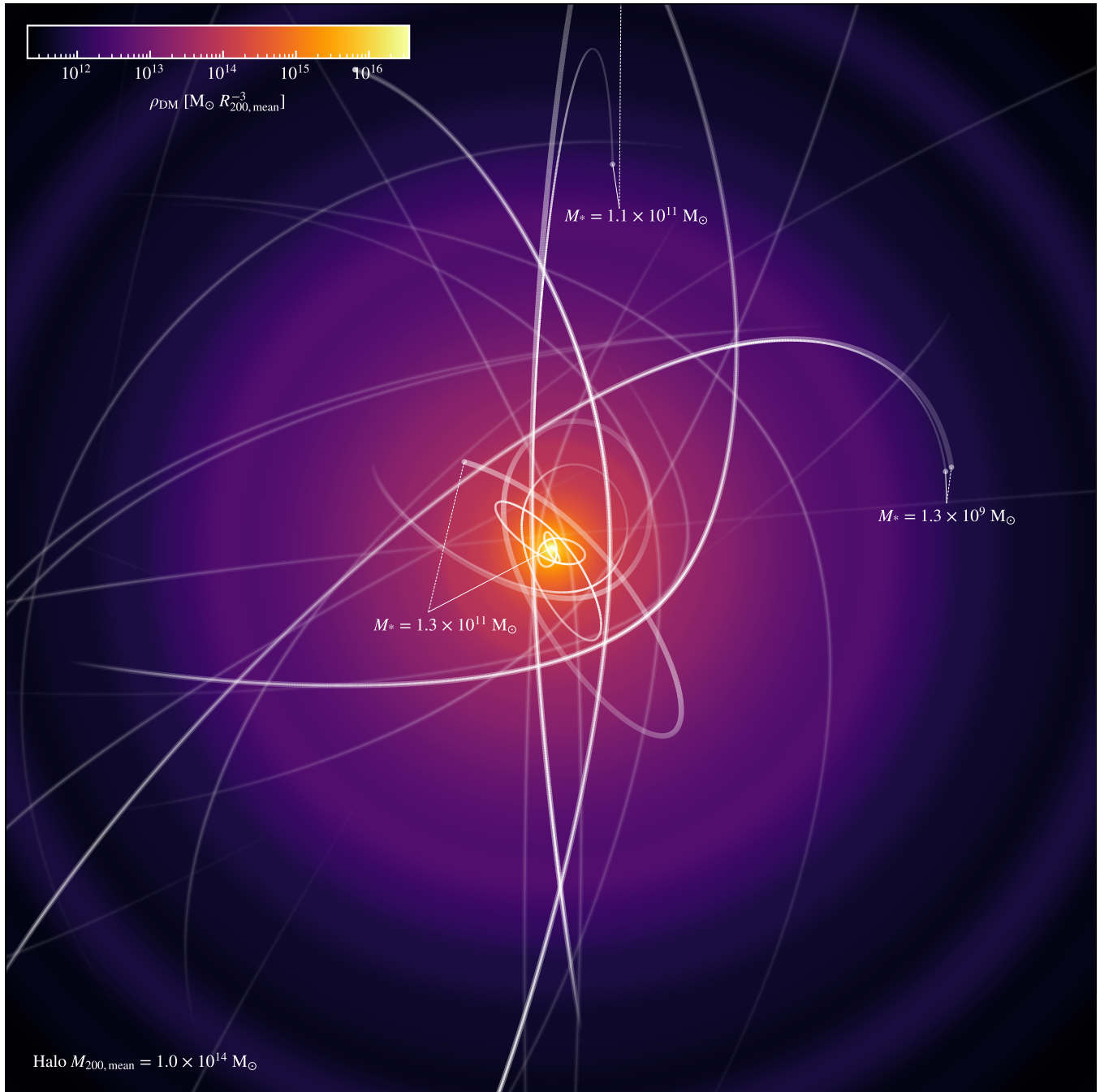


FIG. 1.— Shows selected galaxy orbits, evolved for 10 Gyr in a cluster. The background colour shows the cluster’s spherically averaged dark matter density. Orbits for each galaxy are shown with and without dynamical friction enabled; those with dynamical friction are shown by brighter and thinner lines. The transparency of a line at a given position depends on its distance into the page. Selected galaxy masses are labeled, with solid and dashed lines connecting the labels to the final positions of the galaxies with and without dynamical friction, respectively.

during the first orbital period, and only for galaxies with halo masses above 0.1 times the mass of the cluster. [Dacunha et al. \(2022\)](#) investigated IllustrisTNG and, while they generally attributed the decreasing splashback radii to dynamical friction, noted that DF could not explain why increases in galaxy brightness above $i < -19.4$ did not produce additional decreases in the splashback radius. A similar insensitivity to galaxy magnitude was found by [More et al. \(2016\)](#).

Recently, [O’Neil et al. \(2022\)](#) find, also using IllustrisTNG, that the discrepancy between splashback radii measured through dark matter and galaxies depends on the absolute subhalo mass, rather than the mass ratio between the subhalo

mass and total halo mass (as expected with the effects of DF), ultimately arguing that selection effects among galaxies are more likely the cause of the smaller-than-expected splashback radii.

Observationally, [Chang et al. \(2018\)](#) found that high luminosity galaxies traced out smaller R_{sp} , which is consistent with either the expected influence of dynamical friction or galaxy selection effects; however, they also found this effect to be small and within their measurement uncertainty. [Murata et al. \(2020\)](#) did not find consistent trends in splashback radius values with varying magnitude cuts.

The issue of dynamical friction’s influence in galaxy clus-

ters – particularly on measurements of the splashback radius – is thus a topic that is often discussed, but has not often been deeply studied. Large volume cosmological simulations involve dynamical friction as a result of N-body dynamics. This means that dynamical friction cannot be separated from the other gravitational forces. To target dynamical friction, we must run idealised simulations without the effect at all. In this paper, we seek to address this question by evolving simulated galaxy clusters with an analytical implementation of dynamical friction, allowing the role of dynamical friction to be isolated and clearly understood. The rest of the paper is structured as follows. Section 2 outlines our methods, including the implementation of dynamical friction and the simulations (Sec. 2.3). Our results are described in Section 3, and conclusions are shown in Sec. 4.

2. METHODS, OBSERVATIONS, SIMULATIONS ETC.

In this work we use data from the IllustrisTNG (TNG) cosmological simulations to reconstruct simplified realizations of clusters and subhaloes before evolving the subhalo orbits further forwards in time. We use cluster information from TNG because, although we create an idealized simulation to test DF, the initial phase-space distribution of the subhaloes is crucial for replicating the splashback radius. Creating a realistic phase-space distribution of subhaloes organically is very difficult, and it is easy to inadvertently destroy the splashback radius, which reflects billions of years of the cluster’s evolution. These complications are why we use the TNG data instead of creating our own clusters, even if that approach could, in theory, be more flexible. The next sections introduce TNG (2.1) and how (sub)haloes in TNG are identified and selected (2.2), before describing the details of our simulation (2.3) and fitting procedure (2.4).

2.1. IllustrisTNG Simulations

We utilize the $z = 0$ snapshot of the largest-volume IllustrisTNG cosmological simulations, as introduced by Nelson et al. (2018); Pillepich et al. (2018a) and publicly released in Nelson et al. (2019). Though the full TNG simulation series includes three box sizes (approximately 50, 100, and 300 Mpc side lengths), we use the highest-resolution of the largest volume runs, labeled as TNG300-1. TNG300-1 has a periodic box with side length 302 Mpc, providing a large sample of galaxy clusters. This volume contains 2500^3 dark matter particles with masses of $5.9 \times 10^7 M_\odot$, and 2500^3 gas particles with target cell masses of $1.1 \times 10^7 M_\odot$. The dark matter particles have a gravitational softening length of 1.5 kpc in co-moving units for $z > 1$ and physical units for $z \leq 1$, whereas the gas cells utilize an adaptive softening length (minimum 0.37 kpc).

TNG is built on the magnetohydrodynamical (MHD) moving-mesh code Arepo (Springel 2010), with an updated version of the Illustris galaxy formation model (Vogelsberger et al. 2013). In the model, gas cells cool through radiative processes and metal line cooling, until they stochastically form stars. As the stars evolve, stellar winds and supernovae return mass, energy, and enriched metals to the gas. Black holes are also included in the simulation; they are seeded in haloes with masses of $1.2 \times 10^6 M_\odot$. TNG updates parts of the Illustris model, including radio mode feedback from active galactic nuclei (AGN) (Weinberger et al. 2017), new supernova wind model (Pillepich et al. 2018a), and also includes improvements to the numerical convergence of Arepo (Pakmor et al. 2016).

$\log M_{200,\text{mean}}/M_\odot$	13-13.5	13.5-14	14-14.5	> 14.5
N_{halo}	770	394	185	51
$N_{\text{subhalo}}/10^6$	3.29	5.65	8.52	7.88
$N_{\text{galaxy}}/10^5$	3.49	6.36	9.93	9.38

TABLE 1

THE NUMBER OF HALOES AND SUBHALOES, AS WELL AS SUBHALOES WITH STELLAR MASS EXCEEDING $10^7 M_\odot$ (GALAXIES), FROM THE TNG300-1 SNAPSHOT AT $z = 0$, SEPARATED INTO 0.5-DEX BINS BY HALO MASS.

See Weinberger et al. (2017) for more information about other AGN feedback modes.

IllustrisTNG follows a cosmology consistent with the Planck Collaboration et al. (2016) results. All the runs use cosmological parameters of $\Omega_m = \Omega_{dm} + \Omega_b = 0.3089$, $\Omega_b = 0.0486$, and $\Omega_\Lambda = 0.6911$. Additionally, we use $\sigma_8 = 0.8159$, $n_s = 0.9667$. The Hubble constant is set as $H_0 = 100h \text{ km s}^{-1} \text{ Mpc}^{-1}$, with $h = 0.6774$ (Planck Collaboration et al. 2016). Some runs are dark-matter (gravity) only, and the rest are fully hydrodynamical runs. We utilize the hydrodynamical runs.

2.2. Halo selection and galaxy definition

We follow the halo selection criteria of O’Neil et al. (2021), choosing all haloes of $M_{200,\text{mean}} > 10^{13} M_\odot$. Beyond the mass requirement, O’Neil et al. (2022) additionally remove haloes that are within $10R_{200,\text{mean}}$ of a more massive halo, preferentially selecting haloes that are isolated and have not been disrupted. This filter is important given that we care about the density profiles outside of the cluster center, and because further simulations of the cluster (see Section 2.3) are based on isolated spherical potentials for each halo. From this process we were left with 1401 haloes at $z = 0$. However, we further filter the most massive halo because we identify its density profile as having been significantly disrupted by some less massive haloes within $10R_{200,\text{mean}}$, producing a final sample of 1400 haloes.

Table 1 shows how the 1400 haloes are split by mass, as well as their constituent subhaloes. Subhaloes were identified with the SUBFIND algorithm (Springel et al. 2001) and linked with a Friends-of-Friends algorithm using $b = 0.2$. Subhalo properties (e.g. position) are defined relative to the center of the halo, which is located at the most bound particle in the halo. Of these subhaloes, we identify a “galaxy” as any subhalo with stellar mass greater than $10^7 M_\odot$.

2.3. Simulation details

Using the haloes and subhaloes identified in the TNG300-1 data, we reconstruct the clusters, relying on on version 1.9 of the GALPY package as outlined in Bovy (2015)¹. GALPY, among other capabilities, provides the ability to build a gravitational potential and integrate orbits within that potential.

For each cluster in the sample, an enclosed mass profile was constructed in 100 bins, spaced logarithmically from 0.01 to $5R_{200,\text{mean}}$. The profile accounts for the dark matter, gas, and stellar matter, in the TNG snapshot. This enclosed mass profile was then interpolated and transformed to a spherically symmetric potential (arbitrary scaling constants were set with $\text{ro} = 1 \text{ kpc}$ and $\text{vo} = 1 \text{ kms}^{-1}$). All subhaloes within $15R_{200,\text{mean}}$ were also reconstructed in GALPY, treating them

¹ GALPY is open source and available for use by the community: <http://github.com/jobovy/galpy>

as point particles for the gravitational calculation. From the TNG group catalogues, we include the stellar and total bound mass, positions, velocities, and half-mass radii (used for the DF calculation) of subhaloes. Together, this information was used to reconstruct the cluster and integrate orbits using the 5-4 Dormand-Prince integrator (“dopr54_c”) in GALPY.

The subhaloes are integrated in the static gravitational potential of the cluster for 10 Gyr, with the subhalo positions outputted every 1 Gyr. The simulation was run twice from the same starting conditions. In one case, we run with the gravity from a static cluster potential as the only force, in which case there is no dynamical friction implemented. In the second, we run the GALPY integration with both the cluster potential and a dynamical friction force, which is described in the next section.

2.3.1. Analytical implementation of dynamical friction

Dynamical friction is implemented in GALPY using an analytical approximation based on Chandrasekhar’s dynamical friction formula (Chandrasekhar 1943) and closely following the implementation of Petts et al. (2016). The specific representation that galpy uses is written as:

$$\mathbf{a}(\mathbf{x}, \mathbf{v}) = -2\pi G^2 M \rho(\mathbf{x}) \ln(1 + \Lambda^2) \cdot \left(\text{erf}(X) - \frac{2X}{\sqrt{\pi}} \exp(-X^2) \right) \frac{\mathbf{v}}{v^3}. \quad (1)$$

This expression gives the acceleration of an object of interest, with mass M , position \mathbf{x} , and velocity \mathbf{v} , moving through a background medium of density ρ . The term X is written by,

$$X = \frac{v}{\sqrt{2}\sigma_r(r)}, \quad (2)$$

where σ_r is the radial velocity dispersion.

One term of Chandrasekhar’s formula whose execution frequently varies is the Coulomb logarithm term $\ln(\Lambda)$. Λ is related to the ratio of impact parameters b_{\min}/b_{\max} , but writing this quantity in terms of system quantities is difficult (see Just & Peñarrubia (2005) for a discussion of the complexity). In Section 3.2.2 we investigate the role of the Λ term, but GALPY defaults to:

$$\Lambda = \frac{r/\gamma}{\max(r_{\text{hm}}, GM/v^2)}, \quad (3)$$

where γ is a scaling term, r is the radial distance of the subhalo from the center at any given point, and r_{hm} is the half-mass radius of the subhalo. We use the default $\gamma = 1$. For the vast majority of galaxies in our simulation, $r_{\text{hm}} > GM/v^2$.

For the simulations run with dynamical friction, the acceleration is recalculated at every numerical timestep. Each subhalo’s half-mass radius and total mass is used in calculating the acceleration, but like the positions and velocities, these are held constant and not updated throughout the simulation.

2.4. Bootstrapping and fitting

We create galaxy number density profiles for each cluster (see Section 3.2.1 for more discussion). This entails sorting the galaxies by distance from the cluster center and separating them into 32 bins spaced logarithmically from $0.1 - 10^{0.8} R_{200, \text{mean}}$. The count of galaxies in each bin divided by the volume of that bin is the density profile.

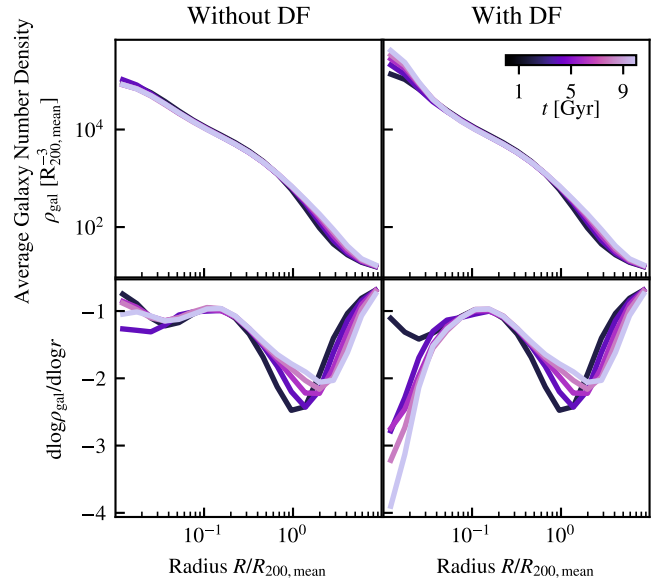


FIG. 2.— Time evolution of average galaxy number density profiles (upper) and differential density profiles (lower) through 10 Gyr of evolution, as shown in the colourbar. The profiles are evolved with DF disabled (on left) and enabled (on right). Haloes are stacked with $M_{200, \text{mean}}$ between 10^{14} and $10^{14.5} M_{\odot}$ (184 haloes), and include all subhaloes.

We then take the logarithmic derivative of these profiles, and the minimum of that profile is the splashback radius. To measure the splashback radius in a robust way and quantify uncertainty, we first bootstrap the density profiles and fit them.

For bootstrapping, we provide the density profiles for a given set of clusters (divided by mass) and (sub)set of subhaloes. We bootstrap 1000 times, with 32 sub-bootstraps, and return bootstrapped density profiles and logarithmic density profiles, as well as errors.

To improve quality of the fits, we scale all of the density profiles before bootstrapping. As reference, we use our sample with halo mass between 10^{14} and $10^{14.5} M_{\odot}$ and with minimum subhalo stellar mass cut of $10^7 M_{\odot}$, and no dynamical friction, since the fitting code works best for this sample. We compute the average density profile for the reference sample and the sample of interest, and find an average scale factor between them. We then multiply all profiles by that factor, while preserving the shape of the density profile. Doing so reduces residual trends where the splashback radius moves inward with increased subhalo mass, and allows for fixed initial free parameters and ranges to be used throughout.

The 1000 bootstrapped profiles are fit with open-source fitting code from O’Neil et al. (2022), using fits based on theoretical density profiles from Diemer & Kravtsov (2014), where the overall density is comprised of an inner, outer, and transition region:

$$\rho(r) = \rho_{\text{inner}} \times f_{\text{trans}} + \rho_{\text{outer}}. \quad (4)$$

The above components can be written as:

$$\rho_{\text{inner}} = \rho_s \exp\left(-\frac{2}{\alpha} \left[\left(\frac{r}{r_s}\right)^{\alpha} - 1\right]\right), \quad (5)$$

$$f_{\text{trans}} = \left[1 + \left(\frac{r}{r_t}\right)^{\beta}\right]^{-\frac{\gamma}{\beta}} \quad (6)$$

$$\rho_{\text{outer}} = \rho_m \left[b_e \left(\frac{r}{5R_{200, \text{mean}}}\right)^{-s_e} + 1 \right], \quad (7)$$

We adjust the fitting boundaries from Appendix B of O’Neil et al. (2021) so that we fit ρ_{inner} at radii $0.2 < r/R_{200,\text{mean}} < 1.2$, with outer fit extending from $2.0 < r/R_{200,\text{mean}} < 10.0$. The transition region is fit from $1.0 < r/R_{200,\text{mean}} < 2.0$, so there is some overlap between the inner and transition regions during fitting. The lack of mergers in our simulation does not have an effect on the splashback radius measurement as the minimum inner radius for fitting is $0.2R_{200,\text{mean}}$.

We discard all fits that do not have a minimum value less than -3 in the differential density profile, as they generally do not trace the splashback curve, as seen by eye. Because our splashback radius values are higher than the typical values measured, (see Figure 5, this is simply because of the way R_{sp} is defined), the fitting code may preferentially seek low values of the splashback radius. With these adjustments, we are confident in the quality of fits. Visual confirmation suggests that the fits across halo and subhalo mass cuts are accurate.

3. RESULTS

Figure 1 illustrates the wide variation in how the orbits of galaxies are affected by dynamical friction. Certain galaxies are greatly affected, spiraling into the dense cluster center, while others experience only moderate changes to their orbits. Many seemingly do not undergo any notable changes, such as the galaxies shown more faintly in the background. The galaxies shown in this figure are not representative of the population as a whole, and were selected to demonstrate this variety. Galaxies with properties leading to higher drag forces (galaxies that approach the cluster center closely, are more massive, have higher values of Λ , etc.) are shown to be more affected by DF. In Figure 1, given the labeled stellar masses, the highlighted galaxies have masses approaching or exceeding the widely used $M_{\text{subhalo}}/M_{\text{halo}} \gtrsim 1\%$ metric, where DF is expected to become influential (Adhikari et al. 2016; More et al. 2016).

These examples illustrate the qualitative impact of dynamical friction on individual galaxy orbits, but to understand how dynamical friction affects our inference of galaxy cluster properties, like the splashback radius, we must expand our analysis to a large sample. The splashback radius is marked by the minimum in the dip of the differential density profile, shown in the bottom panels of Figure 2, which shows the time evolution of galaxy number density and logarithmic density profiles with and without dynamical friction, summed over many clusters. Measurements of R_{sp} are defined relative to $R_{200,\text{mean}}$, because the outskirts of clusters are most self-similar when stacked by $R_{200,\text{mean}}$ (Diemer & Kravtsov 2014; Lau et al. 2015; Shi 2016; Umetsu & Diemer 2017).

The density profile does not evolve dramatically over 10 Gyr, but the differential density profile does exhibit more significant changes with time evolution. The gradual outward creep of the splashback radius, regardless of DF implementation—growing by approximately a factor of two throughout the simulation—does not represent a physical change in the cluster. Because we do not model continuous accretion of mass in our potential, the value of $R_{200,\text{mean}}$ used here is fixed at its initial value from $z = 0$. Consequently, as we evolve further into the future, $R_{200,\text{mean}}$ becomes increasingly underestimated relative to the simulated satellite accretion. Further, as shown in O’Neil et al. (2023) and O’Neil et al. (2024), the dip in the differential density profile is created by galaxies with infall times typically over 5 Gyr ago, leading to some small offsets in our simulated properties. As we are generally only concerned with the influence of dynamical friction, we are still able to compare the two

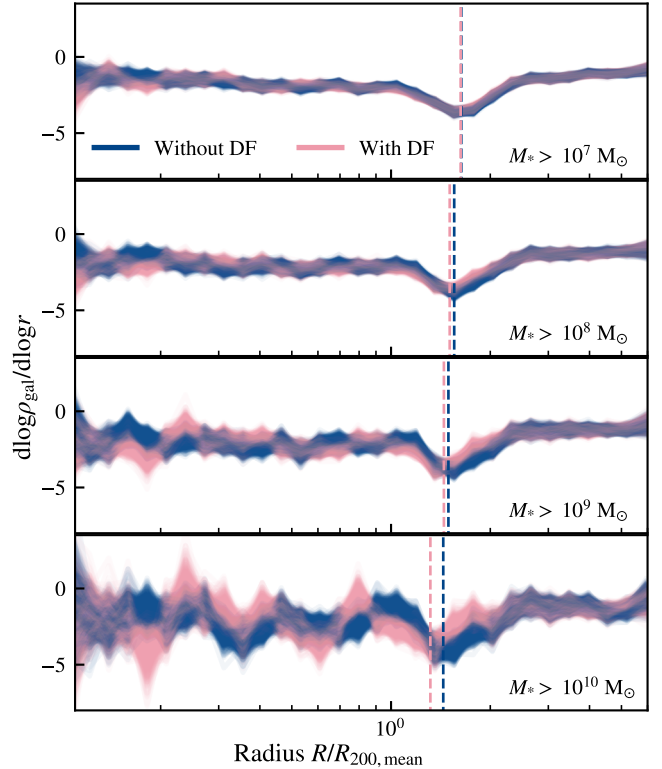


FIG. 3.— Bootstrapped, unfitted differential density profiles for haloes of $M_{200,\text{mean}}$ between 10^{13} and $10^{13.5} M_{\odot}$ evolved for 5 Gyr, among subhaloes with minimum stellar mass cuts, as labeled in each panel. Profiles evolved without DF are shown in blue, and those with DF are shown in pink. Vertical dashed lines mark the respective median splashback radius, in matching colours.

simulations to each other and so this shift is not problematic.

With DF enabled, there is a visible overdensity at the center ($\leq 0.1R_{200,\text{mean}}$), that grows with time, which is consistent with the orbital decay that dynamical friction produces. In a real cluster, these galaxies may merge with the central cluster galaxy (e.g. Ostriker & Hausman 1977); however, this simulation does not have a mechanism for mergers, and therefore these galaxies continue to orbit close to the center. Even though this central impact is clear, the influence of dynamical friction on the splashback region in particular ($\sim R_{200,\text{mean}}$) is not apparent by eye.

To quantify the splashback radius, we bootstrap the density profiles for stacked clusters, as described in Section 2.4. We look at the cluster after 5 Gyr of evolution as at least one crossing time has passed, which we require for the splashback radius to ‘update’ (Figs. 3 through 6 are all at $t = 5$ Gyr). Throughout, we divide the clusters into 0.5-dex mass bins for $\log M_{200,\text{mean}}/M_{\odot}$ in the ranges 13.0 - 13.5, 13.5 - 14.0, 14.0 - 14.5, and above 14.5. Figure 3 shows the bootstrapped differential density profiles, with increasing stellar mass cuts for the subhaloes.

The strength of dynamical friction, as a result of many gravitational interactions, is determined by the subhalo’s total mass rather than its stellar mass. However, throughout our work we present results as a function of stellar mass rather than total mass. We do so because in observation, the limiting factor about whether a galaxy is detected is more closely related to its stellar mass than its total mass. Therefore dividing our galaxy sample by stellar mass allows our simulation to be more easily connected to observational constraints.

The profiles are shown before fitting, producing increased

M_*/M_\odot	10^7	10^8	10^9	10^{10}
$\bar{M}_{\text{subhalo}}/M_\odot$	1.5×10^{10}	5.6×10^{10}	1.6×10^{11}	4.8×10^{11}
$M_{\text{subhalo}}/M_\odot$	10^{10}	10^{11}	10^{12}	10^{13}
\bar{M}_*/M_\odot	0	1.7×10^8	2.1×10^{10}	1.2×10^{11}

TABLE 2

THE TOP TWO ROWS SHOW MEDIAN (BARRED QUANTITY) SUBHALO TOTAL MASS AMONG THE ENTIRE SELECTED SAMPLE OF TNG300-1 HALOES FOR THE LISTED STELLAR MASSES. THE BOTTOM ROWS SHOW THE INVERSE, WITH MEDIAN STELLAR MASS AMONG OUR CLUSTER SAMPLE FOR GIVEN SUBHALO MASSES.

noise – with increased scatter visible as the subhalo sample size shrinks. Even so, Figure 3 visually demonstrates the impact that dynamical friction has on the differential density profiles. Where the profiles appear more blended, dynamical friction has had a weaker effect on the profile. The dip corresponding to the splashback radius is clearly visible, and matches well with the vertical dashed line that identifies the median splashback radius for the sample (post-fitting), such that our visual interpretations here relate well to the quantitative discussion later on.

At less massive stellar mass cuts ($M_* > 10^7 M_\odot$) the profiles with and without DF are highly blended. Greater subhalo minimum stellar mass cuts produce increased divergence between the simulations run with and without dynamical friction. We only include minimum mass cuts, rather than i.e. both maximum and minimum masses. Still, because the subhalo mass function can be modeled by a power law with negative slope, most galaxies above a minimum mass cut are close to that minimum mass (e.g. we expect the profile with $M_* > 10^7 M_\odot$ to be dominated by galaxies with $M_* \sim 10^7 M_\odot$). As the stellar mass cut increases, both minima move inward (which will be discussed further later), but the profiles with dynamical friction are more significantly shifted towards smaller radii. The changes in the profile, across minimum stellar mass cuts, correspond with the widening separation in the median splashback radius. Notably, this plot examines only the lowest-mass clusters, for which we see the greatest influence of dynamical friction.

After bootstrapping and fitting, we extract values of the splashback radius from the minima of each fitted logarithmic density profile, producing posterior distributions such as the one shown in Figure 4, which shows a histogram of splashback radius distributions for the lowest mass clusters from the bootstrapped and fitted profiles, following the procedure outlined in Section 2.4. That the recorded splashback radii trace a normal distribution indicates that our fitting procedure is stable (e.g. there are no significant outliers and the distribution is not bivariate). Dynamical friction reduces the splashback radius, significantly among high mass galaxies but barely if all galaxies are included (the black curves). As expected, higher galaxy mass cuts correspond with stronger reductions in the splashback radius because of dynamical friction.

However, there is a significant residual trend towards smaller splashback radius as galaxy mass increases, even without dynamical friction. The source of this trend is unclear, but it impacts primarily the lowest-mass clusters (see Figure 5). Because our fit quality for the bootstrapped profiles in this mass bin is high and has been verified by eye, we do not believe it results from a fitting issue. It is possible that the high-mass galaxies trace a different dynamical path than other galaxies, which appears more prominently among the lower-mass clus-

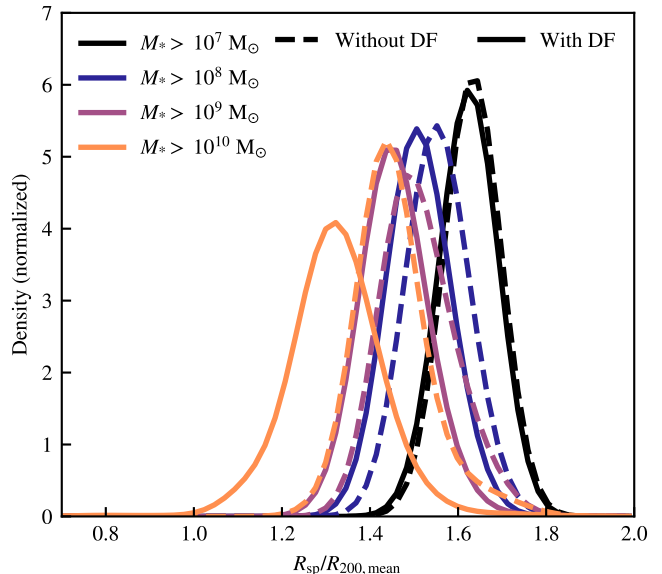


FIG. 4.— Splashback radius distributions after 5 Gyr for haloes with masses of $10^{13} < M_{200,\text{mean}}/M_\odot < 10^{13.5}$. Minimum stellar mass cuts are shown in different colors. Distributions without dynamical friction are marked with dashed lines, while those evolved with dynamical friction use solid lines.

ters.

Our galaxy samples are also greatly affected by the output of the TNG clusters at $z = 0$, as they form the initial conditions of our simulations. O’Neil et al. (2022) worked with the same sample of haloes and subhaloes, and found similar, but larger, trends at $z = 0$ (0 Gyr). We have examined the “contamination” of our sample at 5 Gyr (i.e. what fraction of galaxies within $2R_{200,\text{mean}}$ at 5 Gyr were inside that radius at the start of our simulation), to see how these galaxies, which primarily trace the splashback radius, might be more or less affected by the starting conditions. However, this contamination fraction is relatively constant across cluster masses. Consequently, we cannot conclude that the R_{sp} measurements of lower mass clusters are particularly impacted by the simulation starting conditions.

O’Neil et al. (2022) found an $> 30\%$ variation in R_{sp} between stellar mass cuts of 10^7 and $10^{10} M_\odot$ for their lowest mass clusters, and $\sim 20\%$ for the highest mass clusters. We, after 5 Gyr, find a reduced $\sim 15\%$ difference for the lowest mass clusters and little residual discrepancy for the highest mass clusters. Thus, we may simply demonstrate a lingering, but pre-existing, trend, which started more strongly for lower mass clusters.

We are interested in how these trends persist across cluster masses. Figure 5 shows splashback radius distributions, separated by cluster halo mass and subhalo stellar mass. DF reduces the splashback radius, with more prominent effects among subhaloes of higher stellar mass and for clusters of lower mass ($< 10^{14} M_\odot$). These results are consistent with the qualitative trends expected of dynamical friction, with high-mass subhaloes in low-mass haloes primarily affected.

In the literature, a variety of approaches, mostly in simulation, have been used to find the minimum mass fraction ($M_{\text{subhalo}}/M_{\text{halo}}$) that is required for dynamical friction to have a significant impact on the subhalo orbit. We expect that a significant alteration of the orbit will correspond to a change in the splashback radius. Though the subhalo mass is the dynamically relevant quantity, we express our results in terms of stellar mass because it is far more relevant for observations.

In order to compare to the literature we must understand how the stellar mass and subhalo mass are connected. The stellar mass-halo mass relation has been broadly studied (Mitchell et al. 2016, e.g.) and examined in IllustrisTNG as well (Pillepich et al. 2018b). With our sample of galaxies, we find that stellar mass cuts correspond to median subhalo masses as outlined in Table 2, which are consistent with results from O’Neil et al. (2024). There is a slight dependence of the subhalo mass to stellar mass on cluster mass, with M_{subhalo}/M_* as a function of stellar mass decreasing for greater cluster mass. However, the trend is consistent between cluster masses ($M_{\text{subhalo}} \propto M_*^{0.5}$), and are all well within 1σ , so only the overall median is presented here.

Work by van den Bosch et al. (1999) performed N-body simulations of an isothermal halo with Milky Way-like mass $\sim 10^{12} M_\odot$, and studied eccentricities of orbiting objects. They found DF timescales to be Gyr-scale, and that DF is negligible for satellites with mass under $10^9 M_\odot$, producing a mass fraction requirement of $M_{\text{subhalo}}/M_{\text{halo}} > 0.1\%$. They argue that this 0.1% figure scales for galaxy clusters, while assuming that cluster timescales are equivalent to the Milky Way simulation timescale. Therefore they expect dynamical friction to matter only for subhaloes of total mass $> 10^{12} M_\odot$, within a hypothetical cluster of mass $10^{15} M_\odot$. A subhalo mass of $10^{12} M_\odot$ corresponds to a stellar mass of $\sim 2 \times 10^{10} M_\odot$ (see Table 2). Using a cut of $M_* > 10^{10} M_\odot$ for our most massive cluster bin, we do not see a significant reduction in R_{sp} , suggesting that a mass fraction above 0.1% may be required.

More recent work by van den Bosch et al. (2016), however, argues that a mass ratio of 10% is necessary for dynamical friction to notably alter an orbit, among haloes of mass $\geq 10^{13} M_\odot$. They examine three different cosmological simulations (from the Bolshoi and Chinchilla suites) with varying cosmological parameters and mass resolutions. They find this mass fraction requirement across all three simulations. The 10% figure is consistent for our findings in the high cluster-mass regime. For example, among our most massive clusters, ($\sim 10^{15} M_\odot$) we would expect DF to be impactful only for stellar mass cuts exceeding $7 \times 10^{11} M_\odot$. We thus would not expect to find significant differences for any of the stellar mass cuts shown in Figure 5, and we do not. On the other end, for a cluster of mass $10^{13} M_\odot$ in our sample, we would require a minimum stellar mass of $\sim 2 \times 10^{10} M_\odot$ for DF to have an impact. We do see a significant ($\geq 1\sigma$) reduction in the splashback radius for a cut of $M_* > 10^{10} M_\odot$ after 5 Gyr, suggesting that the requirement of van den Bosch et al. (2016) may be too stringent. However, direct comparison is challenging because they did not divide their sample by halo mass. They, additionally, account for processes such as tidal stripping that contribute to subhalo mass loss, which are excluded from our study. Hence, it is expected that a higher starting mass fraction would be required if mass loss processes are included, because mass loss should reduce the strength of dynamical friction.

Yet other studies have found that a mass fraction of 1% is the requirement for dynamical friction to have an impact on subhaloes (Adhikari et al. 2016; More et al. 2016). Adhikari et al. (2016) examined clusters of virial mass $\geq 10^{14}$, and subhaloes with radial plunging orbits. They found the splashback radius was reduced by up to $\sim 20\%$ for low-mass clusters ($3 - 5 \times 10^{13} M_\odot$) between subhaloes with masses less than-versus exceeding $4 \times 10^{11} M_\odot$, which corresponds to a stellar

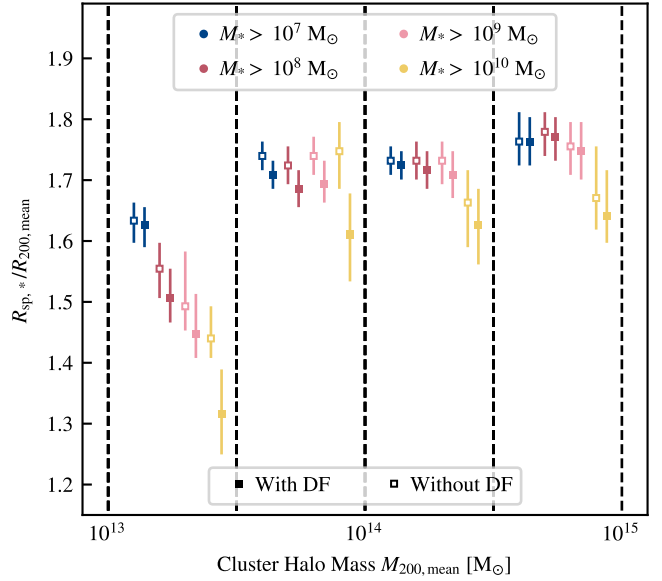


FIG. 5.— Splashback radius distributions after 5 Gyr from bootstrapped and fitted profiles, divided by halo mass groups of 0.5-dex (separated by vertical black dashed lines.) Within each halo mass division, horizontal position is unconnected to mass. Minimum subhalo stellar mass cuts are individually coloured. Median splashback radii calculated from haloes evolved without DF are shown with unfilled square markers, while those evolved with DF are shown with filled squares. The error bars show the 16-84 percentile of the range of each distribution.

mass cut of $\sim 3 \times 10^9 M_\odot$. In the matching cluster mass bin ($10^{13.5} \leq M_{200,\text{mean}}/M_\odot < 10^{14}$), we find only a 7% reduction in the splashback radius, even using a stellar mass cut of $10^{10} M_\odot$. We do not find as significant a reduction as Adhikari et al. (2016) for that case. Plunging radial orbits (as used in Adhikari et al. (2016)) should introduce the most extreme case of DF, so it is unsurprising that their subhaloes are more affected than those of this simulation. They also find that DF has a reduced effect in lower-concentration clusters, bringing their results closer to ours. Future work could examine the role of cluster concentration with the IllustrisTNG sample, using our more physically motivated subhalo orbits.

The wide variation in literature mass fractions reinforces the need for numerical simulations to ascertain the complex dependence of DF on subhalo mass, size, position, velocity, as well as halo density. We generally find that requiring $M_{\text{subhalo}}/M_{\text{halo}} > 1\%$ captures our results, though again, we find that M_*/M_{halo} is a more useful metric. For clusters of mass greater than $10^{14} M_\odot$, a reduced splashback radius should be traced only by galaxies with stellar masses exceeding $10^{10} M_\odot$, consistent with Figure 5.

Figure 5 again shows variation in splashback radius as a function of increased galaxy stellar mass, even without dynamical friction (as seen most clearly in the dashed lines of Figure 4). Quality control on the fits has reduced that variation for higher-mass haloes. However, this trend still exceeds 1σ between $M_* > 10^7$ and $M_* > 10^{10}$ for the lowest-mass haloes in our sample ($10^{13} < M_{200,\text{mean}}/M_\odot < 10^{13.5}$). Since our simulations are idealized and, other than dynamical friction, only include gravitational forces between the cluster potential and individual subhalo, we attribute this residual trend to fundamental differences in the phase-space characteristics of massive galaxies, which are stronger in the less massive clusters.

Though these variations in R_{sp} are interesting, we are pri-

marily interested in the discrepancies between the simulations run with and without dynamical friction. To this end, Figure 6 shows the ratio of the splashback radii with and without dynamical friction, but as a function of minimum subhalo stellar mass over halo mass. By looking at the overlapping points, we can see that despite the residual trends seen in Figs. 4 and 5, there is very good agreement when we examine the fraction $R_{\text{sp,DF}}/R_{\text{sp,NoDF}}$. Therefore we conclude that any contamination of our sample does not significantly affect our analysis of dynamical friction.

It is only after this mass fraction ($M_*/M_{200,\text{mean}}$) exceeds 10^{-4} that we see notable decreases in the splashback radius ($\sim 10\%$) due to DF, which is consistent with our estimates and the figure produced by Adhikari et al. (2016). We also note that, as expected, the mass fraction is what drives the trend here, not only the subhalo mass cut or cluster mass. However, O’Neil et al. (2021) showed that in the TNG simulations it was the absolute subhalo mass that matters for the decrease in splashback radius, again indicating that dynamical friction cannot be the only reason for those offsets. This difference is particularly of note since we use the same sample as O’Neil et al. (2021).

Compared to previous simulations, Fig. 6 suggests that dynamical friction alone cannot account for the discrepancies found in McAlpine et al. (2022), who use a stellar mass cut of $10^8 M_\odot$ and see a $\sim 10\%$ reduction in splashback radius, or O’Neil et al. (2021), who found a $\sim 12\%$ discrepancy between dark matter and galaxy splashback radii for cluster masses of $10^{13} - 10^{13.5} M_\odot$, but used a subhalo *total* mass cut of $10^9 M_\odot$. Diemer (2017) state that dynamical friction can reduce splashback radius measurements up to 20%, which exceeds the maximal reduction that we find.

Most observing projects use cluster masses generally above $10^{14} M_\odot$ (More et al. 2016; Chang et al. 2018; Shin et al. 2019, e.g.). For such surveys, regardless of the magnitude limitations, dynamical friction should not significantly influence the measured splashback radius. Magnitude cuts in surveys will preferentially select more luminous galaxies that are expected to be more massive, which may enhance the impact of dynamical friction. For e.g. Chang et al. (2018), they have an apparent magnitude cut of $i = 21.5$, which at $z = 0.55$ corresponds to an i -band absolute magnitude of -21 . Using the magnitude-mass diagram for TNG galaxies, the Chang et al. (2018) sample has a minimum stellar mass of $10^{10} M_\odot$ (O’Neil et al. 2021). Even with such high stellar masses, for these halo masses ($\langle M_{200,\text{mean}} \rangle = 2.5 \times 10^{14} M_\odot$), DF does not produce a $> 1\sigma$ effect on the splashback radius.

3.1. Residence Time

The splashback radius is traced out by subhaloes that have spent sufficient time in the cluster to reach their first apocenter. In position-radial velocity phase space, then, R_{sp} should appear as an overdensity of subhaloes with low radial velocities. Moreover, galaxies that are just infalling into the cluster should not trace out the splashback radius. In this section, we investigate how the cluster phase-space evolves with residence time.

The phase-space distributions for high-stellar mass galaxies ($M_* > 10^9 M_\odot$) are shown in Figure 7 after 10 Gyr of evolution, for our lowest-mass clusters (between 10^{13} and $10^{13.5} M_\odot$). We examine the phase space after 10 Gyr, rather than 5 Gyr like in the rest of the analysis, to see longer-duration changes in the cluster environment. We separate the subhaloes

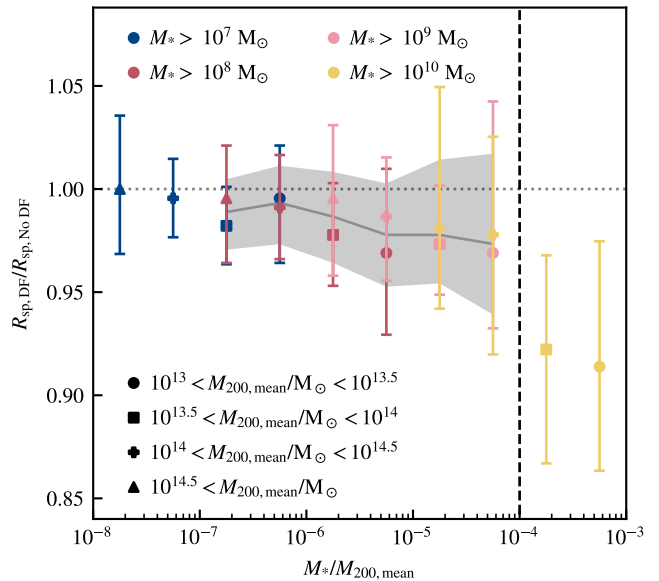


FIG. 6.— The ratio of the splashback radius with and without dynamical friction, after 5 Gyr, for the ratio of minimum stellar mass to halo mass (measured in the middle of the bin). The horizontal grey dotted line marks a ratio of 1 (i.e. no difference). The black dashed line shows where $M_{\text{subhalo}}/M_{200,\text{mean}} \approx 0.01$. Finally, the solid grey line and shaded band show average ratio and error for the regions with multiple data points.

by residence time, which is defined as the time since the subhalo first crossed inside of $R_{200,\text{mean}}$ in 10 Gyr of simulation. The top three panels show subhaloes with residence times of 1 to 3 Gyr, 4 to 6 Gyr, and 7 to 10 Gyr. The bottom panel shows all galaxies meeting the mass cut, including galaxies that never reach within $R_{200,\text{mean}}$ or galaxies that began the simulation inside $R_{200,\text{mean}}$. We filter out a small number of galaxies with $M_{\text{subhalo}} > 0.05 M_{200,\text{mean}}$, as they should, in a physically realistic environment, influence the movement of the cluster. On the plot they would appear as a horizontal band throughout a range of radial positions with very low radial velocities (approximately zero).

If instead a minimum stellar mass cut of $10^7 M_\odot$ is applied, the velocity profiles resemble the expected distribution from IllustrisTNG outputs (see e.g. Dacunha et al. 2022; O’Neil et al. 2024), suggesting our model is reasonably realistic, with respect to other simulated clusters (e.g. the large number of infalling galaxies with negative radial velocity, the dispersal of galaxies at long residence times). For galaxies with residence times between 1 and 3 Gyr, we see the infalling and outgoing galaxies combined, as well as a turnaround in phase space around ~ 5 Gyr.

The splashback feature is thought to be found among galaxies with residence times of order one crossing time (~ 5 Gyr, from O’Neil et al. (2024)), with radial velocities around 0. We begin to see these tracer galaxies in the middle residence time bin, and the number grows with residence times of over 7 Gyr (the top panel). While one might expect the splashback feature to be traced by galaxies with residence times of closer to 5 Gyr, the feature is in fact most visible among galaxies that have spent longer in the cluster (residence time between 7 and 9 Gyr). We attribute this phenomenon to weaker gravitational forces in the least-massive clusters producing less plunging orbits.

The majority of galaxies in this halo sample never reach inside of $R_{200,\text{mean}}$ (approximately 88% for both with and without DF.) Of the galaxies that do, the influence of dy-

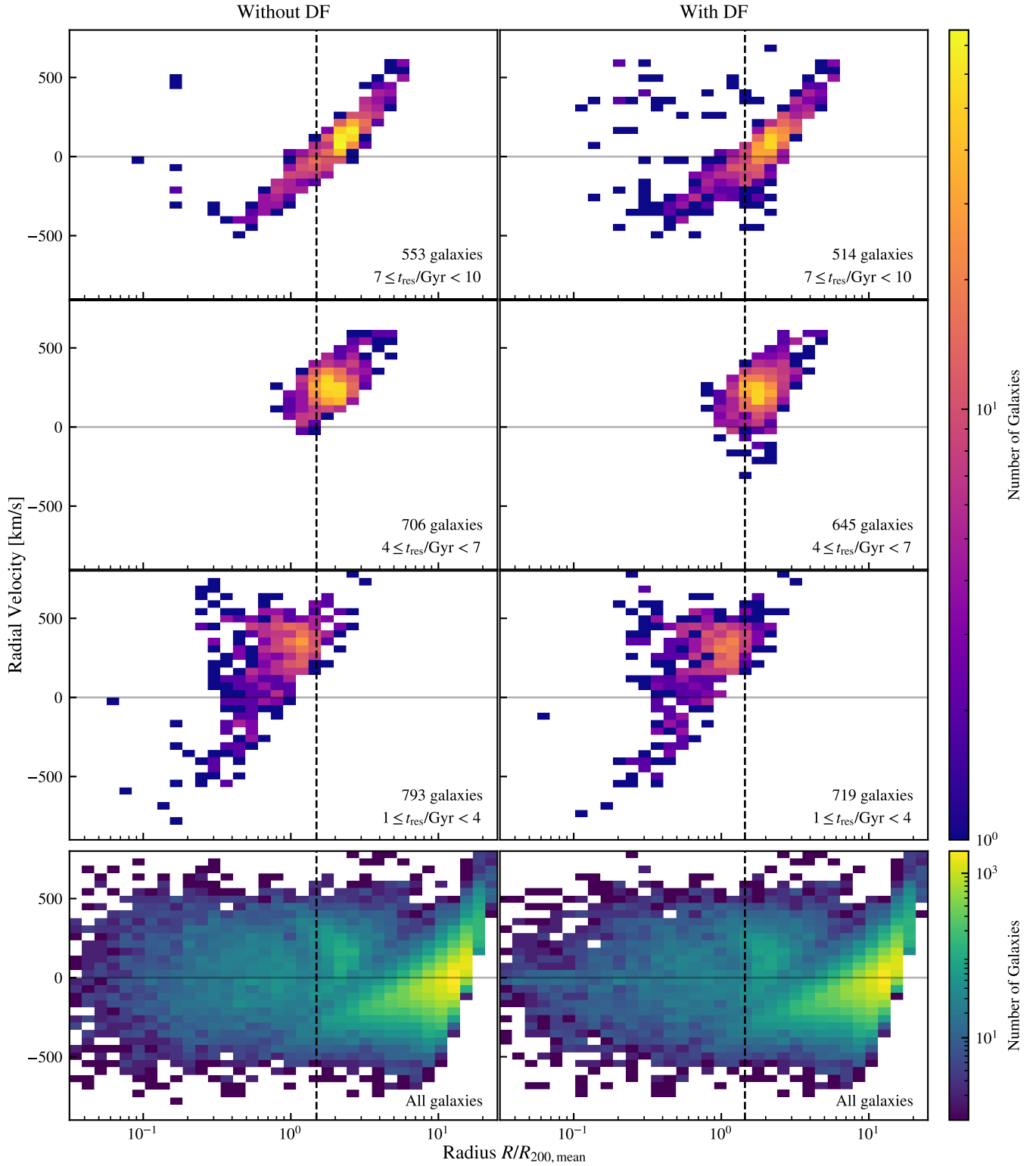


FIG. 7.— 2D histograms of radial velocity and radius plots after 10 Gyr of evolution, with (right column) and without (left) dynamical friction, for the lowest mass haloes ($10^{13} - 10^{13.5} M_{\odot}$, totaling 770 haloes) and subhaloes with minimum stellar mass $M_* = 10^9 M_{\odot}$. Subhaloes with $M_{\text{subhalo}} > 0.05 M_{200,\text{mean}}$ are also excluded. The top three panels are separated by residence time in the cluster, which is calculated from the first time at which the galaxy reaches a position within $R_{200,\text{mean}}$. The bottom row shows the histogram for all subhaloes with $M_* > 10^9 M_{\odot}$ and $M_{\text{subhalo}} < 0.05 M_{200,\text{mean}}$, totaling over 47,000 galaxies. The black dashed line shows the median splashback radius with and without dynamical friction (as measured in Figure 5).

namical friction is most apparent among the galaxies with longer residence times. There are few differences between the phase-space distributions for galaxies with $t_{\text{res}} < 4$ Gyr. By the longest residence time bin, though, the splashback radius (marked with a vertical dashed line) appears slightly reduced. The distribution of radii at $v_r \approx 0$ is wider with dynamical friction enabled as well, matching the wider bootstrapped R_{sp} distributions shown in Figure 8.

A small number of galaxies with $v_r < 0$ and $4 \leq t_{\text{res}} < 7$ appear only with dynamical friction enabled. By comparison to the phase-space distribution with a lower mass cut, it is apparent that (essentially) only galaxies with high masses exist in this region of phase space, and only when dynamical friction is acting. We can thus see how DF, for a small number of high mass galaxies, dramatically affects their orbital properties (e.g. as visualized in Fig. 1). However, despite these cases, it is also clear that the phase-space distributions are not, overall, dramatically altered with dynamical friction enabled.

3.2. Validation Tests

The use of these idealized simulations, and the analytical implementation of dynamical friction, allows us to uniquely isolate DF. However, the analytical implementation of DF includes approximations not present in an N-body approach. Therefore, in the following section we investigate the robustness of our results.

3.2.1. Bin Widths

When bootstrapping and fitting the density profiles (see Section 2.4), binning is an important criteria to consider. We use the standard logarithmically spaced bins to ensure that the inner bins are well-sampled. Ideally, the splashback radius distributions should not vary with the number of bins used. Independence from binning indicates that the measurements are not residual effects of the binning choices, and instead reflect real variations in measurements of R_{sp} . Too small a number of bins may wash out real variations in R_{sp} measurements, while the use of too many bins produces noisy data due to poorly sampled bins.

Various bin densities are used throughout the literature for splashback radius studies. Different sources cover a different radius range, but for studying R_{sp} , they typically go out to ~ 5 - $10 R_{200,\text{mean}}$, ranging from 15 logarithmically spaced bins (Murata et al. 2020; Dacunha et al. 2022), to 32 (O’Neil et al. 2022), 40 (McAlpine et al. 2022), and 42 (linear spacing) (O’Neil et al. 2021).

In Figure 8 we show a violin plot of the splashback radius distribution as a function of number of bins used in the bootstrapping and fitting process, to check the resilience of our results to binning. We apply our fitting procedure as outlined in Section 2.4. In the top panel, including all galaxies with stellar mass above $10^7 M_{\odot}$, the distributions are narrow and similar between the different binning options (i.e. left to right), indicating we are very accurately measuring the splashback radius. For the bottom panel, the sample of subhaloes is greatly reduced, producing greater error in the bootstrapping and fitting processes. We selected this subset of cluster and subhalo masses as they involved some of the most extreme density profile variation, and most challenging fits. The broader and more varied distributions reflect the greater uncertainties involved. The cluster subset includes 770 haloes, but of the 3.3×10^6 subhaloes with stellar masses above $10^7 M_{\odot}$, only approximately 21,000 have $M_* > 10^{10} M_{\odot}$. Above 32 bins,

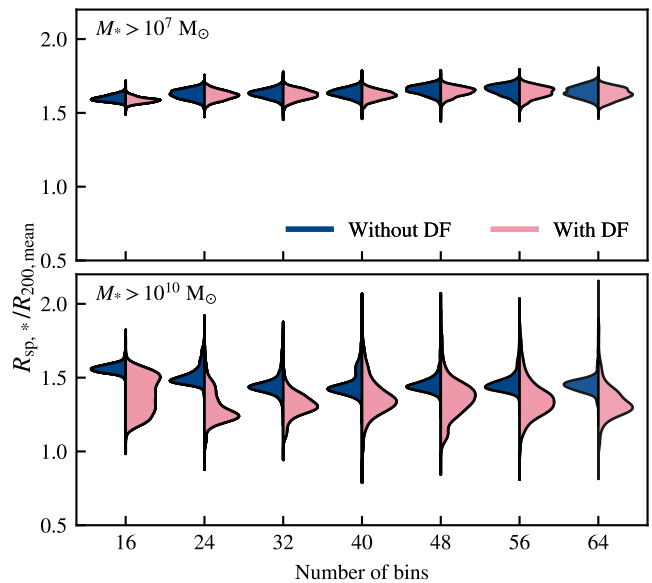


FIG. 8.— Violinplots of splashback radius distributions for a varying number of logarithmic radius bins, among haloes of $10^{13} < M_{200,\text{mean}} < 10^{13.5} M_{\odot}$, and for subhaloes of stellar mass greater than $10^7 M_{\odot}$ (upper panel) and $10^{10} M_{\odot}$ (lower panel). The distributions evolved without DF are shown on the left in blue, while those with DF are shown on the right in pink.

the distributions appear relatively stable, however, fits judged by eye appeared to decline in quality above 40 bins. Therefore, we use 32 bins for all other data presented throughout.

3.2.2. Constant Coulomb logarithm simulations

As outlined in Section 2.3.1, the Λ term in Chandrasekhar’s analytical DF formula is not particularly well-defined. In the previous sections, we have used the default GALPY implementation of Λ , which is computed as in Equation (3). Here, we seek to investigate how strongly the Λ term affects the dynamical friction term and the R_{sp} measurement.

Boylan-Kolchin et al. (2008) and Jiang et al. (2008) found that merging timescales calculated from the analytical Chandrasekhar formulation are underestimated, relative to results from N-body and hydrodynamic numerical simulations, with Jiang et al. (2008) particularly citing the Λ term as a source of uncertainty. Thus, we expect our results, if anything, generally overestimate the impact of DF.

In general, some DF implementations instead utilize an unchanging Λ related to the scale size of the halo, R_{halo} . However such strategies less accurately match results from N-body simulations (Just & Peñarrubia 2005); specifically, the use of a constant Λ produces overly rapid inspirals and unphysical circularization of orbits Hashimoto et al. (2003). Instead, Petts et al. (2015) use a maximum impact parameter of the subhalo’s orbital radius, which forms the basis for the GALPY implementation. Petts et al. (2015) note that this method can overly amplify the influence of dynamical friction.

Given these uncertainties, we examine the dependence of our results on Λ . We do not examine all possible variations of Λ implementation, instead focusing on the use of a constant value as studied in Hashimoto et al. (2003); Just & Peñarrubia (2005). They found that the use of a constant Λ caused subhaloes to inspiral too quickly, which we might expect to reduce the splashback radius.

The starting distributions of $\ln(\Lambda)$, as calculated in Equation (3), are shown in Figure 9, for subhaloes beginning within $R_{200,\text{mean}}$ at $z = 0$. We select only these subhaloes because they

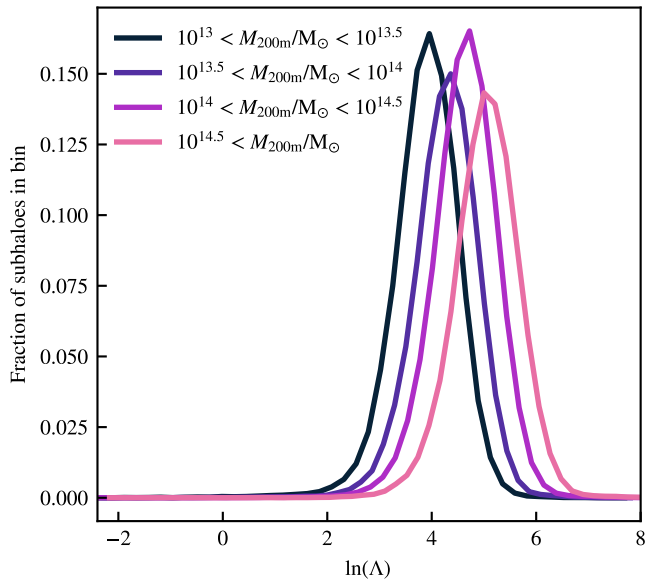


FIG. 9.— Distributions of $\ln(\Lambda)$ for all subhaloes within $R_{200,\text{mean}}$ at the start of the simulation, grouped by halo mass. The histograms are scaled by the number of subhaloes.

are the ones most strongly influenced by dynamical friction (see e.g. Figure 7). We find that $\ln(\Lambda)$ is normally distributed around $\ln(\Lambda) \approx 4 - 5$. The trend towards greater Λ among higher-mass clusters may be unintuitive; since we find DF to be less influential in those clusters, we might expect $\ln(\Lambda)$ to be smaller. However, the larger Λ distributions among high mass cluster are reflective of the larger scale radii of the more massive clusters, i.e. $R_{200,\text{mean}}$ is larger in more massive clusters. (Note again, we found that $r_{\text{hm}} > GM/v^2$ for most galaxies in the simulation, so r_{hm} is the overwhelmingly the value used to calculate Λ , and it does not change greatly with halo mass.) The gravitational forces are simply far stronger in higher-mass clusters, reducing the relative importance of dynamical friction.

To test the impact of Λ , we implement a set of constant- Λ simulations. We evolve all haloes for 10 Gyr as before, but with fixed $\ln(\Lambda)$ values of 2, 5, and 10 for each subhalo. Figure 10 shows how the splashback radius, measured again after 5 Gyr, evolves with Λ for selected halo and subhalo masses. As expected, as $\ln(\Lambda)$ increases, the splashback radii decrease, especially for low-mass haloes. More massive haloes see little impact from adjustments of Λ , even when they exceed the median starting value by more than a factor of two. We attribute this to the relative weakness of DF compared to gravitational forces, such that significantly increasing DF has very little effect on the overall splashback distribution. Interestingly, even with a $\ln(\Lambda) = 2$, which is smaller than the starting median value, the splashback radius is slightly reduced (though not significantly). That finding is consistent with previous work stating that using a constant Λ contributes to overly rapid inspiral and enhanced dynamical friction (Hashimoto et al. 2003; Just & Peñarrubia 2005). Nonetheless, our simple examination into the complexities and uncertainties in defining Λ , suggest that variations in Λ cannot easily account for the splashback radius discrepancies seen in high-mass clusters.

4. CONCLUSIONS

Values of the splashback radius, when measured through galaxy number density, have been found to be smaller than splashback radius measurements made from dark matter pro-

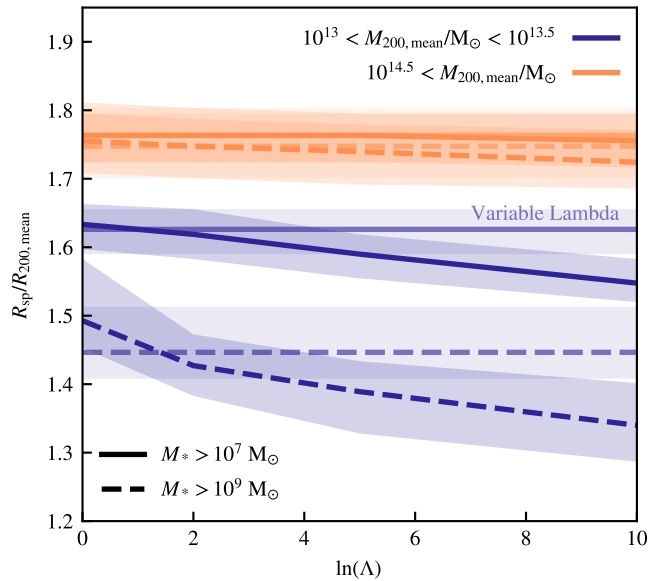


FIG. 10.— Median splashback radius distributions for constant Λ systems, after 5 Gyr of evolution. Low and high mass haloes are included (purple and orange lines, respectively, as marked), with various stellar mass cuts (above $10^7 M_\odot$ in solid lines and $10^9 M_\odot$ dashed). Systems with no dynamical friction are shown at $\ln(\Lambda) = 0$. The lightened lines show the position of the median splashback radius from the default variable implementation of dynamical friction (as used in Figures 2 to 9.). The shaded bands show the 16-84 percentile range for all data.

files (on $\geq 10\%$ scales). This trend persists between observations and simulations. Dynamical friction has been proposed as a force that would uniquely impact the orbits of galaxies, without affecting the dominant, but diffuse, background components of the halo.

Here, we present the results of idealized simulations of galaxy clusters, with dynamical friction implemented analytically through Chandrasekhar’s formula (Chandrasekhar 1943), in order to examine the impact of dynamical friction. The cluster gravitational potentials and subhaloes are initially drawn from the IllustrisTNG cosmological simulation at $z = 0$ to ensure that their properties (e.g. phase-space distribution of subhaloes, mass distribution, etc.) are relatively physical. Subhaloes were then evolved for 10 Gyr twice: both within the cluster’s gravitational potential, and once with the analytical dynamical friction force. We thus isolate dynamical friction, and focus on how the presence of dynamical friction affects the splashback radius of the cluster when measured through the subhalo number density. In particular, we find that:

- Dynamical friction shifts the location of the observed splashback radius, R_{sp} , inwards. We find a *maximal* reduction of the splashback radius because of DF to be approximately 10%. However, we do not expect measurements of R_{sp} to be significantly shifted for clusters of $M_{200,\text{mean}} \geq 10^{14} M_\odot$. Therefore many observational measurements of the splashback radius that find lower-than-expected values of R_{sp} should not attribute discrepancies to dynamical friction.
- The impact of DF on the splashback radius increases, as expected, with the fraction of subhalo (stellar) mass to halo mass (see Fig. 6), as opposed to the subhalo mass, reinforcing the findings of O’Neil et al. (2022) that dynamical friction can not be the sole source of

disagreements between dark matter and galaxy number density profiles.

- Dynamical friction has a greatest effect on galaxies with longer residence times. To what degree these galaxies contribute to the splashback feature partially determines the influence of DF. Among low-mass clusters (e.g. $10^{13} < M_{200,\text{mean}}/M_{\odot} < 10^{13.5}$), the splashback radius is best traced by galaxies with residence times exceeding 7 Gyr, further reducing the measured R_{sp} .
- The Coulomb logarithm term, $\ln(\Lambda)$, is a source of uncertainty in the Chandrasekhar dynamical friction implementation. To test the resilience of our results, instead of adjusting γ , we artificially adjusted, and fixed, Λ . We find that increasing this logarithm reduces the splashback radius, because it strengthens the dynamical friction force. However, we observe significant changes in the splashback radius only for fixed $\ln(\Lambda)$ values of 10 in the lowest mass clusters ($10^{13} < M_{200,\text{mean}}/M_{\odot} < 10^{13.5}$), which is over twice the median starting value of $\ln(\Lambda)$ for those clusters (see Figs. 9 and 10). Thus, our results appear consistent even with some variation in $\ln(\Lambda)$. High-mass clusters are even less responsive to adjustments in $\ln(\Lambda)$.

We find that dynamical friction cannot alone account for the many reported cases of reduced splashback radii when measured with galaxy number density (i.e. rather than dark matter density), particularly among the highest-mass clusters that are most commonly studied (see e.g. More et al. 2016; Chang et al. 2018; Shin et al. 2019).

The semi-idealized simulations presented here exclude other processes that affect the orbits of subhaloes inside the cluster and alter the masses of these subhaloes. For example,

processes such as tidal stripping, if they were included, are expected to reduce the impact of dynamical friction as they reduce the masses of subhaloes during infall (van den Bosch et al. 2016, e.g.). Our use of Chandrasekhar’s analytical formula may also overestimate the strength of the dynamical friction (Boylan-Kolchin et al. 2008; Jiang et al. 2008). Each of these factors would further reduce the contribution of DF to splashback radius discrepancies measured in observation or from cosmological simulations.

This investigation targets isolated clusters at $z = 0$. It is well-known that DF plays a significant role in halo mergers, which we do not study here. Measurements of halo splashback radii at higher redshift, with higher concentrations (e.g. Adhikari et al. 2016) or among less relaxed clusters, may be more strongly affected by dynamical friction.

ACKNOWLEDGEMENTS

The authors thank Jo Bovy for their help with GALPY, and for their rapid responses to questions raised on the GALPY GitHub page. The authors also would like to thank Frank van den Bosch for productive discussions during the early stages of the project. TMO acknowledges support through the Beckman Scholars Program by the Arnold and Mabel Beckman Foundation. TMO also thanks the efforts of her Wellesley College advisor James Battat for his support throughout the research process. JB acknowledges support from NSF grant AST-2153201.

DATA AVAILABILITY

The data and code underlying this work are available at: <https://dx.doi.org/10.5281/zenodo.11357381>. All data used for this work is from the publicly available TNG300-1 simulation, and can be found at <https://tng-project.org> (Nelson et al. 2019).

REFERENCES

- Abadi M. G., Moore B., Bower R. G., 1999, *MNRAS*, 308, 947
- Adhikari S., Dalal N., Chamberlain R. T., 2014, *J. Cosmology Astropart. Phys.*, 2014, 019
- Adhikari S., Dalal N., Clampitt J., 2016, *Journal of Cosmology and Astroparticle Physics*
- Adhikari S., et al., 2021, *ApJ*, 923, 37
- Bahé Y. M., et al., 2019, *MNRAS*, 485, 2287
- Baxter E., et al., 2017, *ApJ*, 841, 18
- Blanton M. R., Eisenstein D., Hogg D. W., Schlegel D. J., Brinkmann J., 2005, *ApJ*, 629, 143
- Bluck A. F. L., Maiolino R., Sánchez S. F., Ellison S. L., Thorp M. D., Piotrowska J. M., Teimoorinia H., Bundy K. A., 2020, *MNRAS*, 492, 96
- Borrow J., Vogelsberger M., O’Neil S., McDonald M. A., Smith A., 2023, *MNRAS*,
- Bovy J., 2015, *ApJS*, 216, 29
- Boylan-Kolchin M., Ma C.-P., Quataert E., 2008, *MNRAS*, 383, 93
- Busch P., White S. D. M., 2017, *MNRAS*, 470, 4767
- Chandrasekhar S., 1943, *ApJ*, 97, 255
- Chang C., et al., 2018, *ApJ*, 864, 83
- Chung A., van Gorkom J. H., Kenney J. D. P., Crowl H., Vollmer B., 2009, *AJ*, 138, 1741
- Contigiani O., Hoekstra H., Bahé Y. M., 2019, *MNRAS*, 485, 408
- Crain R. A., et al., 2015, *MNRAS*, 450, 1937
- Dacunha T., Belyakov M., Adhikari S., Shin T.-h., Goldstein S., Jain B., 2022, *MNRAS*, 512, 4378
- Davis M., Efstathiou G., Frenk C. S., White S. D. M., 1985, *ApJ*, 292, 371
- Dekel A., Devor J., Hetzroni G., 2003, *MNRAS*, 341, 326
- Demarco R., et al., 2010, *ApJ*, 725, 1252
- Diemand J., Kuhlen M., Madau P., 2007, *ApJ*, 667, 859
- Diemer B., 2017, *ApJS*, 231, 5
- Diemer B., Kravtsov A., 2014, *The Astrophysical Journal*
- Diemer B., More S., Kravtsov A. V., 2013, *ApJ*, 766, 25
- Dressler A., 1980, *ApJ*, 236, 351
- Dressler A., Shectman S. A., 1987, *AJ*, 94, 899
- Ebeling H., Stephenson L. N., Edge A. C., 2014, *ApJ*, 781, L40
- Genel S., et al., 2014, *MNRAS*, 445, 175
- Gómez P. L., et al., 2003, *ApJ*, 584, 210
- Gunn J. E., Gott J. Richard I., 1972, *ApJ*, 176, 1
- Hashimoto Y., Funato Y., Makino J., 2003, *ApJ*, 582, 196
- Hogg D. W., et al., 2004, *ApJ*, 601, L29
- Jiang C. Y., Jing Y. P., Faltenbacher A., Lin W. P., Li C., 2008, *ApJ*, 675, 1095
- Just A., Peñarrubia J., 2005, *A&A*, 431, 861
- Kauffmann G., White S. D. M., Heckman T. M., Ménard B., Brinkmann J., Charlot S., Tremonti C., Brinkmann J., 2004, *MNRAS*, 353, 713
- Kim K. J., et al., 2022, *arXiv e-prints*, p. arXiv:2207.12491
- Kimble R. A., Davidsen A. F., Sandage A. R., 1989, *Ap&SS*, 157, 237
- Kravtsov A. V., Borgani S., 2012, *ARA&A*, 50, 353
- Larson R. B., Tinsley B. M., Caldwell C. N., 1980, *ApJ*, 237, 692
- Lau E. T., Nagai D., Avestruz C., Nelson K., Vikhlinin A., 2015, *ApJ*, 806, 68
- Li C., Kauffmann G., Jing Y. P., White S. D. M., Börner G., Cheng F. Z., 2006, *MNRAS*, 368, 21
- Mansfield P., Kravtsov A. V., Diemer B., 2017, *ApJ*, 841, 34
- McAlpine S., et al., 2022, *Monthly Notices of the Royal Astronomical Society*
- McNamara B. R., Nulsen P. E. J., 2012, *New Journal of Physics*, 14, 055023
- Mitchell P. D., Lacey C. G., Baugh C. M., Cole S., 2016, *MNRAS*, 456, 1459
- Moore B., Lake G., Katz N., 1998, *ApJ*, 495, 139
- More S., Diemer B., Kravtsov A. V., 2015, *ApJ*, 810, 36
- More S., et al., 2016, *ApJ*, 825, 39
- Murata R., Sunayama T., Oguri M., More S., Nishizawa A. J., Nishimichi T., Osato K., 2020, *PASJ*, 72, 64
- Nelson D., et al., 2018, *MNRAS*, 475, 624
- Nelson D., et al., 2019, *Computational Astrophysics and Cosmology*, 6, 2

- O'Neil S., Barnes D. J., Vogelsberger M., Diemer B., 2021, *MNRAS*, **504**, 4649
- O'Neil S., Borrow J., Vogelsberger M., Diemer B., 2022, *Monthly Notices of the Royal Astronomical Society*
- O'Neil S., Borrow J., Vogelsberger M., Zhao H., Wang B., 2023, *arXiv e-prints*, p. [arXiv:2310.07754](https://arxiv.org/abs/2310.07754)
- O'Neil S., Borrow J., Vogelsberger M., Zhao H., Wang B., 2024, *MNRAS*, Ostriker J. P., Hausman M. A., 1977, *ApJ*, **217**, L125
- Pakmor R., Springel V., Bauer A., Mocz P., Munoz D. J., Ohlmann S. T., Schaal K., Zhu C., 2016, *MNRAS*, **455**, 1134
- Peacock J. A., 1999, *Cosmological Physics*. Columbia University Press
- Peebles P. J. E., 1993, *Principles of Physical Cosmology*. Princeton University Press, doi:[10.1515/9780691206721](https://doi.org/10.1515/9780691206721)
- Petts J. A., Gualandris A., Read J. I., 2015, *MNRAS*, **454**, 3778
- Petts J. A., Read J. I., Gualandris A., 2016, *MNRAS*, **463**, 858
- Pillepich A., et al., 2018a, *MNRAS*, **473**, 4077
- Pillepich A., et al., 2018b, *MNRAS*, **475**, 648
- Planck Collaboration et al., 2016, *A&A*, **594**, A13
- Poggianti B. M., Smail I., Dressler A., Couch W. J., Barger A. J., Butcher H., Ellis R. S., Oemler Augustus J., 1999, *ApJ*, **518**, 576
- Press W. H., Schechter P., 1974, *ApJ*, **187**, 425
- Schaye J., et al., 2015, *MNRAS*, **446**, 521
- Shi X., 2016, *MNRAS*, **459**, 3711
- Shin T.-h., Diemer B., 2023, *MNRAS*, **521**, 5570
- Shin T., et al., 2019, *MNRAS*, **487**, 2900
- Somerville R. S., Davé R., 2015, *ARA&A*, **53**, 51
- Springel V., 2010, *Monthly Notices of the Royal Astronomical Society*
- Springel V., White S. D. M., Tormen G., Kauffmann G., 2001, *MNRAS*, **328**, 726
- Umetsu K., Diemer B., 2017, *ApJ*, **836**, 231
- Vogelsberger M., Genel S., Sijacki D., Torrey P., Springel V., Hernquist L., 2013, *MNRAS*, **436**, 3031
- Vogelsberger M., et al., 2014, *MNRAS*, **444**, 1518
- Vogelsberger M., Marinacci F., Torrey P., Puchwein E., 2020, *Nature Reviews Physics*, **2**, 42
- Vollmer B., Beck R., Kenney J. D. P., van Gorkom J. H., 2004, *AJ*, **127**, 3375
- Weinberger R., et al., 2017, *MNRAS*, **465**, 3291
- Wetzell A. R., Tinker J. L., Conroy C., van den Bosch F. C., 2013, *MNRAS*, **432**, 336
- Khakaj E., Diemer B., Leauthaud A., Wasserman A., Huang S., Luo Y., Adhikari S., Singh S., 2020, *MNRAS*, **499**, 3534
- Zürcher D., More S., 2019, *ApJ*, **874**, 184
- van den Bosch F. C., Lewis G. F., Lake G., Stadel J., 1999, *ApJ*, **515**, 50
- van den Bosch F. C., Jiang F., Campbell D., Behroozi P., 2016, *MNRAS*, **455**, 158

arXiv, making the reviewing process simpler for authors and referees alike. Learn more at <http://astro.theoj.org>.

This paper was built using the Open Journal of Astrophysics L^AT_EX template. The OJA is a journal which provides fast and easy peer review for new papers in the astro-ph section of the